catalysts

MDPI

Article

Strain Engineering for Tuning the Photocatalytic Activity of Metal-Organic Frameworks-Theoretical Study of the UiO-66 Case

Marija Stojković [1] and Igor A. Pašti [1,2,*]

[1] Faculty of Physical Chemistry, University of Belgrade, Studentski trg 12-16, 11158 Belgrade, Serbia; marijastojkovic2212@gmail.com
[2] Department of Materials Science and Engineering, School of Industrial Engineering and Management, KTH–Royal Institute of Technology, Brinellvägen 23, 100 44 Stockholm, Sweden
* Correspondence: igor@ffh.bg.ac.rs; Tel.: +381-11-3336-625

Abstract: In recent years, the class of metal-organic framework (MOF) materials emerged. These materials' unique properties can be ascribed to their structure, containing inorganic nodes connected with organic linkers. Due to their porosity and flexibility, MOFs have become suitable for various energy-related applications, including gas storage, hydrogen production and heterogeneous catalysis, and photocatalysis. Using DFT+*U* calculations, we show that the substitution of metal centers in inorganic nodes and the strain engineering of UiO-66 alters the electronic and optical properties of this material. We show that applying mechanical strain on UiO-66 enables the control of absorption coefficient in the UV-Vis spectrum and the photocatalytic processes' selectivity when reactants for several photocatalytic processes are present. The presented findings could lead to general strategies for designing novel MOFs for sustainable energy conversion applications.

Keywords: metal-organic framework; photocatalysis; band-gap modulation; strain engineering; catalyst selectivity

check for updates

Citation: Stojković, M.; Pašti, I.A. Strain Engineering for Tuning the Photocatalytic Activity of Metal-Organic Frameworks-Theoretical Study of the UiO-66 Case. *Catalysts* **2021**, *11*, 264. https://doi.org/10.3390/catal11020264

Academic Editor: Weilin Dai

Received: 31 January 2021
Accepted: 15 February 2021
Published: 16 February 2021

1. Introduction

In recent years, there has been an ongoing challenge of using clean energy sources. One of the most abundant and versatile clean energy sources is solar energy. There are many possibilities of using this renewable source. In addition to photoelectrochemical and photovoltaic systems [1,2], one of the main uses of solar energy is heterogeneous photocatalysis. The photocatalytic processes include three main steps [3]: (1) absorption of photon, (2) creation of electron-hole pair (exciton) which can migrate to catalytic centers, and (3) redox reactions with substrates.

Regarding these steps in a photocatalytic process, a material used as a photocatalyst should possess strong solar radiation absorption, a very long lifetime of excited states, and good charge mobility to prevent rapid recombination [3,4]. Ever since the discovery of TiO_2 as a suitable catalyst for water photosplitting [5], there has been an expansion in the research and development of new synthetic photocatalysts. The main focus has recently been placed on a new class of materials known as metal-organic frameworks (MOFs) [6,7]. Due to their specific structure, which contains metal nodes connected with organic linkers, MOFs showed great potential for energy storage and conversion-related applications, such as capacitors and Li-ion batteries [8–10]. Different pore sizes inside MOFs and exchangeable building units make this material suitable for gas storage and hydrogen production [11,12]. Moreover, MOFs' high porosity leads to an increased number of active sites, making them convenient for catalytic processes [13], including photocatalytic ones [14–16].

When we look at different MOF structures, we can see that the metal nodes usually consist of monovalent and divalent, as well as trivalent and four valent metals such as Zr^{4+}, Ti^{4+}. The most stable structures often have four valent metals [17]. In that kind of system, metal clusters can contain up to twelve metal ions. When it comes to the connection between the building units, there is great diversity, particularly in materials containing Zr ions. Nevertheless, in these MOFs, clusters are predominantly built from highly symmetrical units in the form of Zr_6O_8. Considering the topology, MOFs can have different numbers of connecting points [6,8,12].

UiO-66 is one of the most investigated MOFs to this day, justified by its chemical, thermal, and mechanical stability [18]. In its original form, it has Zr metal centers and the face-centered cubic structure [19]. Possible modifications of UiO-66(Zr) using either the functionalization of linkers or replacements of Zr centers with other metals were reported [20,21]. Wu et al. [22] systematically investigated the modification of UiO-66(Zr) using both strategies and found that the longer-lived excited states in Ce-based UiO-66, UiO-66(Ce) than in UiO-66 MOFs with other metals, ascribed to the facile charge separation in the case of UiO-66(Ce). The authors further showed that the functionalization of the linkers (1,4-benzene-dicarboxylate) enables modification of the electronic structure of UiO-66(Ce), enabling the tuning of the photocatalytic activity.

Due to very open structures, MOFs belong to the soft materials class [23], and small mechanical strain can be applied to them without irreversible structural changes. Their flexibility was recently employed for the development of strain-based sensors with unprecedented performances [24]. Here we show that the strain engineering in MOFs can be an excellent tool for modifying the electronic structure and the band gap, allowing the modification of optical and photocatalytic properties. For this purpose, we compare the effects of strain on UiO-66(Zr) and UiO-66(Ce), demonstrating the mentioned effects in the latter case. Using mechanical strain, we show that one can exclude undesired photochemical processes and obtain high selectivity, which is a great challenge in practice.

2. Results

2.1. Geometry

The optimized structures of UiO-66(Zr) and UiO-66(Ce) (Figure 1) have triclinic primitive cells with a_0 = 14.834 Å for Zr and a_0 = 15.440 Å for the Ce case.

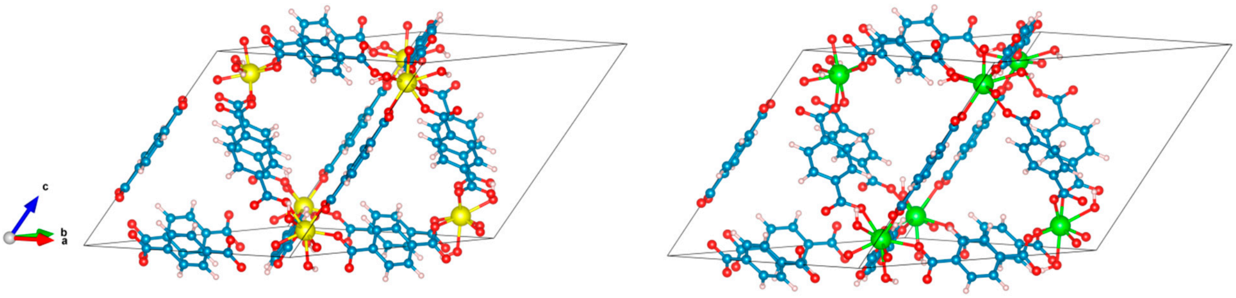

(**a**) (**b**)

Figure 1. (**a**) The optimized structure of the unit cell of UiO-66(Zr); (**b**) the optimized structure of the unit cell of UiO-66(Ce).

This difference is predominantly due to the M–O bond lengths, amounting to 2.216 Å for Zr–O and 2.395 Å for the Ce–O bond. Upon analyzing the optimized structures, we see that the M–O bonds behave differently in these two cases. Namely, the Zr–O bond is rather rigid, and its change upon the application of strain is relatively small. For the applied strain of −3%, the Zr–O bond is changed to 2.191 Å. However, in the Ce case, the Ce–O bond contracts to 2.312 Å. As a result, the optimized structures with the negative strain (contraction, Figure 2) look qualitatively different. In the case of Zr-based MOF, due to the rigidity of the Zr–O bond, the contraction is compensated with the deformation of the linker. In contrast, for the Ce-based MOF, the deformation of the Ce–O bond compensates the applied strain. The situation is similar for the positive strain (expansion of the lattice).

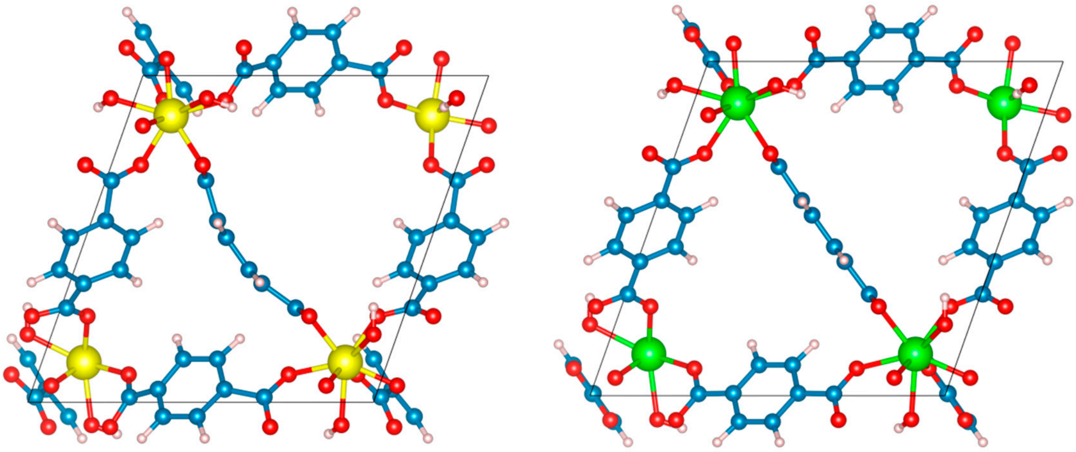

(**a**) (**b**)

Figure 2. (**a**) The optimized structure of the unit cell of UiO-66(Zr) with the applied strain of −3%; (**b**) The optimized structure of the unit cell of UiO-66(Ce) with the applied strain of −3%.

2.2. Electronic Structure

Upon optimizing the crystal structures, we turn to analyzing the electronic structures of studied MOFs (Figure 3). Densities of states (DOS) show a bandgap in all the cases, which is effectively tuned by the applied strain (Table 1). For UiO-66(Zr), the calculated bandgap for the unstrained structure is 2.98 eV, which is lower than the experimental value (3.76 eV [25]) and the HSE06/PBEsol result [22]. This difference is expected due to the level of theory that we have used. For UiO-66(Ce), the HSE06/PBEsol result is 2.66 eV [22]. The DOS profiles agree with the hybrid calculations, showing that for UiO-66(Zr), the Zr 4d states are well above the bottom of the conduction band. However, for UiO-66(Ce), the Ce 4f states form the conduction band. In the case of UiO-66(Ce), the bandgap is much more sensitive to the applied strain. The lattice contraction causes the increase of the bandgap, while the expansion of the lattice decreases the bandgap (Table 1). It is interesting to observe that the applied strain does not cause much change in the Zr 4d states but greatly affects the Ce 4f states, which we will discuss later. As the Ce 4f states form the conduction band, this also reflects on the optical properties of UiO-66(Ce), presented in the next section.

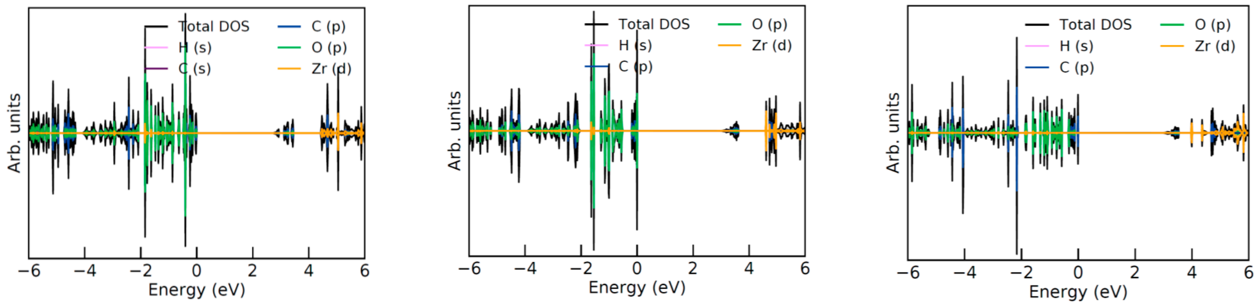

(**a**) (**b**) (**c**)

Figure 3. *Cont.*

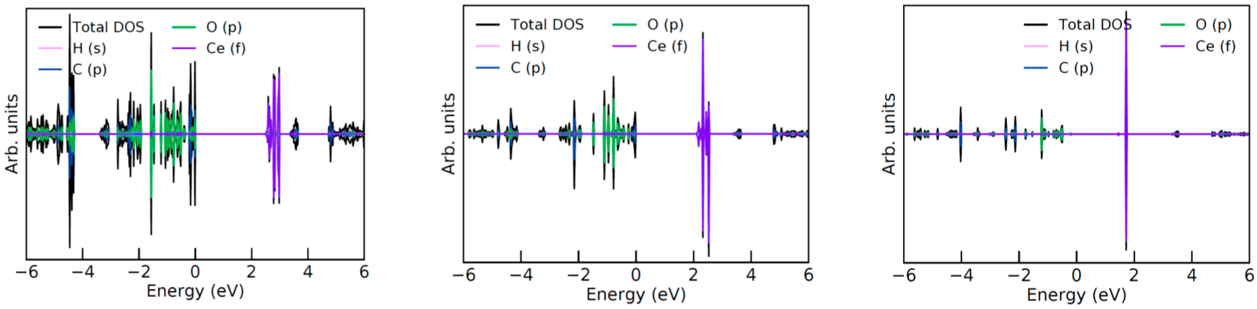

(**d**) (**e**) (**f**)

Figure 3. Densities of states (DOS) of the optimized structures of UiO-66 with different metal centers and applied strain: (**a**) UiO-66(Zr) with the strain of −3%; (**b**) unstrained UiO-66(Zr); (**c**) UiO-66(Zr) with the strain of +3%; (**d**) UiO-66(Ce) with the strain of −3%; (**e**) unstrained UiO-66(Ce); and (**f**) UiO-66(Ce) with the strain of +3%. DOS plots are generated using sumo tools [26].

Table 1. Calculated bandgap for UiO-66(Zr) and UiO-66(Ce) for different strain applied on the lattice unit cell.

Strain/%	**Bandgap/eV**	
	UiO-66(Zr)	**UiO-66(Ce)**
−3	2.71	2.50
−2	2.87	2.40
−1	2.93	2.27
0	2.98	2.09
+1	2.97	1.91
+2	2.97	1.69
+3	2.95	1.45

2.3. *Optical Properties*

UiO-66(Zr) is a white-colored substance with optical absorption below 300 nm and an absorbance maximum around 250 nm [27]. Compared to our result (Figure 4a), the absorption maximum is shifted to higher energy as the experimental bandgap is larger than the one we calculated. However, the qualitative agreement is rather good. As the strain affects the bandgap of UiO-66(Zr) very little (except for the largest negative strain, Table 1), optical spectra are little affected by strain. However, for UiO-66(Ce), the effect of strain on the optical absorption is appreciable. Negative strain (lattice contraction) causes the blueshift of the optical spectra, while the positive strain (lattice expansion) causes the redshift of the optical spectra (Figure 4b). Moreover, the absorption coefficient is larger for UiO-66(Ce) compared to UiO-66(Zr) (Figure 4). Aside from the tuning of the bandgap via applied strain, a possibility to tune the optical absorption using strain is another strong indication that the strain engineering can be applied as a tool for controlling the photocatalytic properties of MOFs.

2.4. *Tuning Selectivity of the Photocatalytic Process via Strain*

Finally, we present the results of the band alignment procedure for UiO-66(Zr) (Figure 5a) and UiO-66(Ce) (Figure 5b). For the standard hydrogen electrode (SHE) absolute value, we took 4.44 eV [28]. The potentials of other redox couples in Figure 5 are then recalculated to the vacuum scale. We note that there is an uncertainty of the value of the absolute potential of SHE, so the final result of the band alignment procedure has an uncertainty of approximately ±0.2 eV [29]. In addition to the potentials of H^+/H_2 and O_2/H_2O couples, we also added the couples corresponding to the CO_2 reduction process, using the summary of standard electrode potentials reported by Wu et al. [22].

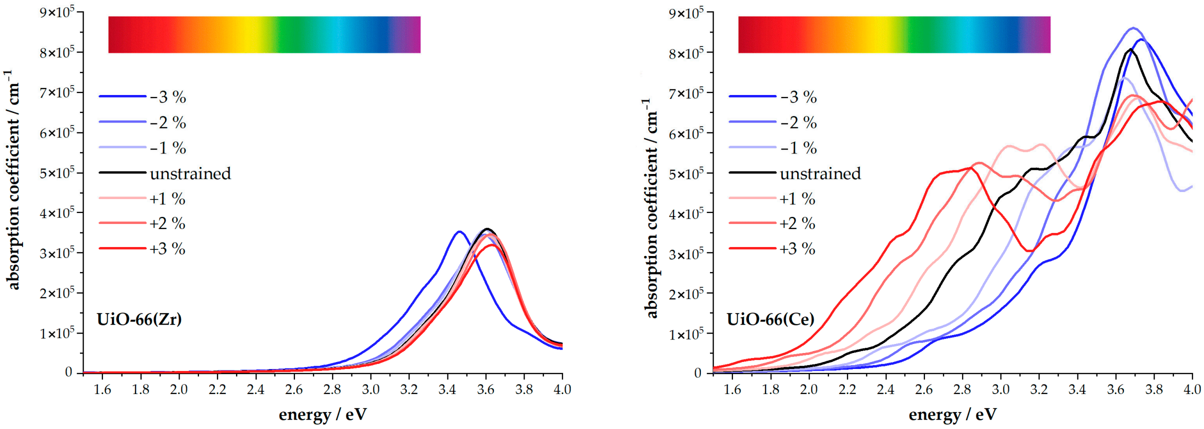

(**a**) (**b**)

Figure 4. Electronic spectra of studied metal-organic frameworks (MOFs) for different values of strain: (**a**) UiO-66(Zr); (**b**) UiO-66(Zr). Insert provides the optical spectra associated with the scale of photon energy.

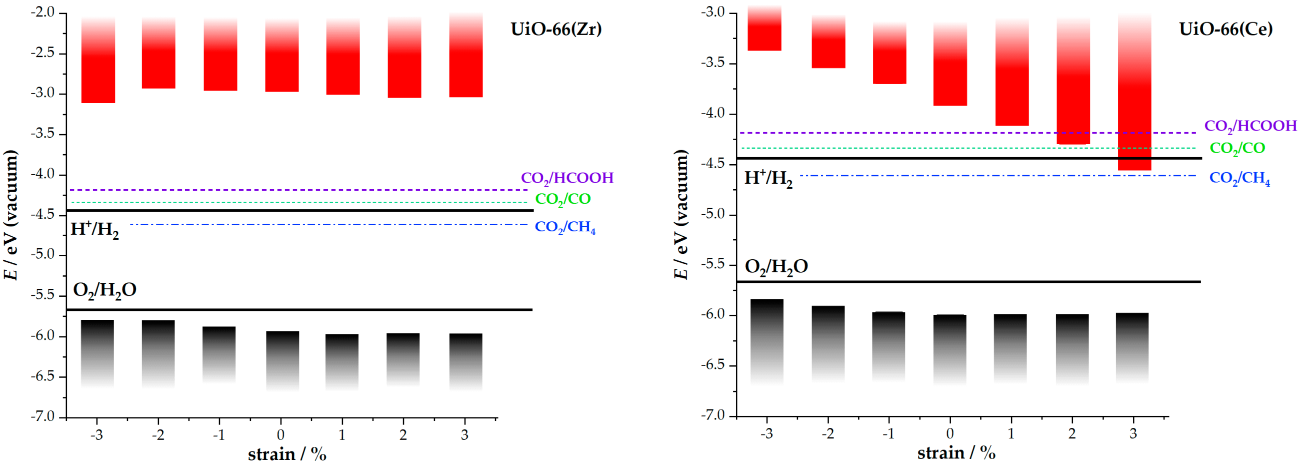

(**a**) (**b**)

Figure 5. Band alignment results for different values of strain: (**a**) UiO-66(Zr); (**b**) UiO-66(Ce). Horizontal lines give redox potentials of H^+/H_2 and O_2/H_2O couples at pH = 0. Dashed lines give the values of indicated redox couples at pH = 7.

We see that the valence band (VB) top is weakly affected by the applied strain for both investigated MOFs. However, for UiO-66(Ce), the conduction band (CB) bottom shifts significantly with the applied strain. This result gives a possibility to tune the photocatalytic activity of UiO-66(Ce) using strain. For example, for the unstrained Ce-based MOF, four reduction processes presented in Figure 5b can occur. However, if a positive strain is applied, the CB bottom shifts downwards, and the processes with more positive redox potentials (at vacuum scale) are switched off one by one. Finally, for the strain of +3%, only the reduction of CO_2 to CH_4 can occur (among presented redox couples), and it is combined with anodic O_2 formation. Such a level of selectivity is generally difficult to obtain, while the use of strain for the control of photocatalytic activity also enables that one material can be used for different processes, which can be switched on or off as desired. This level of control is not possible if other strategies for the control of the catalytic activity are applied, such as chemical modification of the linker.

3. Discussion

As we have shown, the concept of using strain for the control of the electronic structure of MOFs works nicely for the UiO-66(Ce). The induced modifications of the electronic structure reflect onto the optical properties and ultimately the photocatalytic ones. In the case of UiO-66(Ce), a downshift of the CB bottom is seen, and we look into it in more detail. Figure 6 presents DOSes of Ce atoms for different applied strains. As one can see, the f orbitals of Ce atoms degenerate with positive strain, and the band becomes narrower. This occurrence is not seen for the CB of UiO-66(Zr) (Figure 3). If one recalls the results of the structural relaxation of strained structures (Figure 2), it becomes clear that this is due to the variation of the Ce–O bond length. With negative applied strain, the Ce–O bond becomes shorter and causes an upshift of the Ce f states to higher energies, accompanied by removing the Ce f levels' degeneracy. This change in the electronic structure reflects directly on the bandgap and the absolute position of the CB bottom at the vacuum scale.

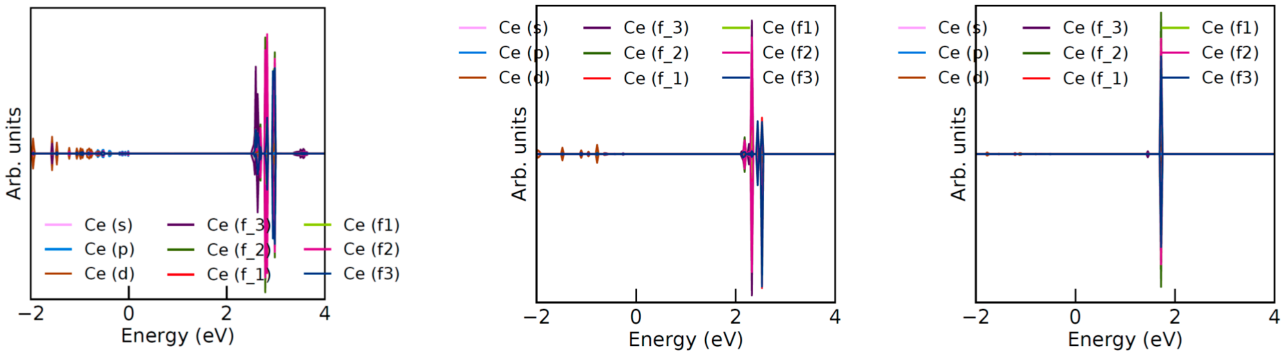

(**a**) (**b**) (**c**)

Figure 6. Densities of states (DOS) Ce atoms in UiO-66(Ce): (**a**) UiO-66(Ce) with the strain of −3%; (**b**) unstrained UiO-66(Ce); (**c**) UiO-66(Ce) with the strain of +3%.

The resulting modifications of the electronic structure of UiO-66(Ce) also have a strong impact on the optical properties (Figure 4). Putting the results in a wider context, it is suggested that mechanical strain can be used to modulate the optical absorption, color and conductivity of UiO-66(Ce). This observation opens the possibility for wider use of UiO-66(Ce), from smart optical materials to strain and chemical sensors. However, we want to link the effects of strain on the photocatalytic activity and selectivity control.

For this purpose, we constructed the 3D diagram showing the dependence of the CB bottom and the VB top positions and the potentials of three selected redox couples (the anodic process is O_2 formation, while reduction processes are H_2 formation and CO_2 reduction to methanol) on the applied strain and pH (Figure 7). We assume that the CB bottom and the VB top positions depend only on the strain, while the redox potentials depend only on pH. H_2 and O_2 evolution processes involve one proton per transferred electron, so the calculated plane slope versus pH axis is 0.059 eV per pH unit. CO_2 reduction to methanol follows the equation:

$$CO_2 + 6e^- + 6H^+ = CH_3OH + H_2O \tag{1}$$

so the slope versus pH axis is also 0.354 eV per pH unit at room temperature. We choose to discuss the CO_2 reduction to methanol due to the importance of methanol in contemporary energy technologies.

As can be seen from Figure 7, pH modulates the relative positions of redox couple potentials vs. the CB bottom of UiO-66(Ce), allowing one to identify the pH-strain domain in which the potential of the H^+/H_2 couple shifts above the CB bottom while the potential of CO_2/CH_3OH couple is still below the CB bottom. In this way, one excluded the H_2 formation, while CO_2 reduction still proceeds. While this discussion only demonstrates the general principle of strain-controlled photocatalysis by UiO-66(Ce), we note that in this particular case, this pH-strain region corresponds to small positive strains for pH just below 7. Hence, as well as altering MOFs (photocatalytic) properties using the change of metal centers and chemical modification of linkers, we suggest that strain should be added to this list and combined with the former two strategies to fully exploit the application potential of MOFs.

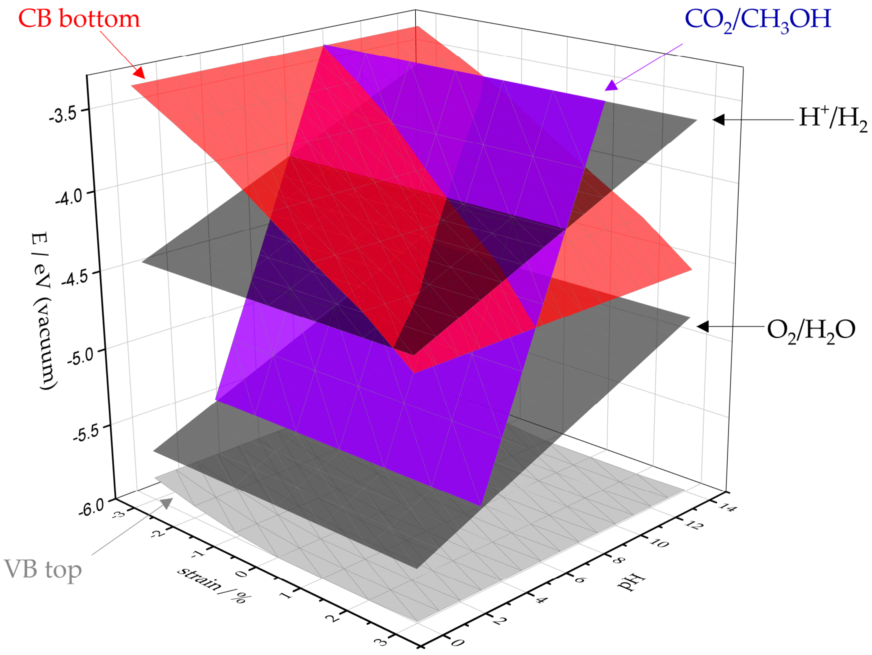

Figure 7. 3D band alignment results for UiO-66(Ce) as the strain and pH function. The potentials of O_2/H_2O, H^+/H_2 and CO_2/CH_3OH couples are included. While the conduction band (CB(bottom and the valence band (VB) top positions depend on strain, the redox potentials depend on pH.

Considering the practical realization of strain-based control of the photocatalytic activity of UiO-66(Ce), or MOFs in general, we have to stress out that this could be rather challenging. However, a first try could be using piezoelectric supports on which thin MOF films are deposited so that the strain can be controlled using the voltage applied to the piezoelectric support. For this strategy, one should build highly adhesive MOF layers with extended crystalline domains so that the grain boundaries do not compensate for the applied strain. Another approach would be the use of architectures similar to those in the membrane-type surface stress sensor used by Yeung et al. [24].

4. Materials and Methods

The first-principles DFT calculations were performed using the Vienna ab initio simulation code (VASP, VASP Software GmbH, Vienna, Austria, version 5.4.4, April 2017) [30–33]. We used the generalized gradient approximation (GGA) in the parametrization by Perdew, Burk, and Ernzerhof [34] and the projector augmented wave (PAW) method [35,36]. The on-site Coulomb interactions were added to the d states of Zr and f states of Ce using the DFT + U scheme of Dudarev et al. [37]. We have systematically investigated the effects of the value of U on the bandgap and opted for U = 6 eV in both cases. The cut-off energy of 500 eV and Gaussian smearing with a width of σ = 0.025 eV for the electronic levels' occupation were used. A Monkhorst–Pack Γ-centered 3 × 3 × 3 k-point mesh was employed for the relaxation calculations. The relaxation of all the atoms in the simulation cell was unrestricted. The relaxation procedure was performed until the Hellmann–Feynman forces on all atoms below 0.01 eV Å^{-1}. Spin-polarization was considered in all of the presented calculations. We used 6 × 6 × 6 k-point mesh for the DOS calculations in combination with the Blöch tetrahedron method [38]. For the band alignment, we used the method of Butler et al. [39] with the same converge criteria for the vacuum potential as in the ref. [22]. Optical spectra were calculated from the frequency-dependent microscopic polarizability matrix in the projector-augmented wave (PAW) methodology [40]. VESTA code was used for visualization [41].

5. Conclusions

We propose the use of strain for the control of the photocatalytic activity and selectivity of MOFs. The general principle is demonstrated for the case of UiO-66(Ce) using DFT + U calculations. While we are aware of the limitations of our theoretical approach, the concept itself shows that the mechanical strain is an eligible tool for controlling MOFs' electronic structure, optical properties, and, ultimately, photocatalytic performance. It is suggested that the combination of strain and pH can be used to control the selectivity of the photocatalytic process to a great extent, as exemplified in the case of CO_2 reduction to methanol. However, the results should be sought in a wider context, as the strain engineering could open a large range of potentially new MOFs applications.

Author Contributions: Conceptualization, I.A.P.; data curation, M.S. and I.A.P.; formal analysis, M.S. and I.A.P.; funding acquisition, I.A.P.; investigation, M.S.; methodology, I.A.P.; visualization, I.A.P.; writing—original draft, M.S.; writing—review and editing, I.A.P. All authors have read and agreed to the published version of the manuscript.

Funding: This research was funded by the Serbian Ministry of Education, Science and Technological Development (grant number not applicable). The computations and data handling were enabled by resources provided by the Swedish National Infrastructure for Computing (SNIC) at the NSC center of Linköping University, partially funded by the Swedish Research Council through grant agreement no. 2018-05973.

Data Availability Statement: The data presented in this study are available on request from the corresponding author.

Conflicts of Interest: The authors declare no conflict of interest.

References

1. Sun, J.; Zhong, D.K.; Gamelin, D.R. Composite photoanodes for photoelectrochemical solar water splitting. *Energy Environ. Sci.* **2010**, *3*, 1252–1261. [CrossRef]
2. Milichko, V.A.; Shalin, A.S.; Mukhin, I.S.; Kovrov, A.E.; Krasilin, A.A.; Vinogradov, A.V.; Belov, P.A.; Simobskii, C.R. Solar photovoltaics: Current state and trends. *Phys.-Usp.* **2016**, *59*, 727–772. [CrossRef]
3. Zhao, S.N.; Wang, G.; Poelman, D.; Van Der Voort, P. Metal Organic Frameworks Based Materials for Heterogeneous Photocatalysis. *Molecules* **2018**, *23*, 2947. [CrossRef] [PubMed]
4. Xiang, Q.; Yu, J. Graphene Based Photocatalysts for Hydrogen Generation. *J. Phys. Chem. Lett.* **2013**, *4*, 753–759. [CrossRef] [PubMed]
5. Hashimoto, K.; Irie, H.; Fijushima, A. TiO_2 Photocatalysis: A historical Overview and Future Prospects. *Jpn. J. Appl. Phys.* **2005**, *44*, 8269. [CrossRef]
6. Rowsell, J.L.C.; Yaghi, O.M. Metal-organic frameforks: A new class of porous materials. *Micropor. Mesopor. Mater.* **2004**, *73*, 3–14. [CrossRef]
7. Hindocha, S. The Chemistry of Metal-Organic Frameworks: Synthesis, Characterization, and Applications. *Johns. Matthey Technol. Rev.* **2017**, *61*, 138–141. [CrossRef]
8. Xia, A.; Mahmood, A.; Zou, R.; Xu, Q. Metal-organic frameworks and their derived nanostructures for electrochemical energy storage. *Energy Environ. Sci.* **2015**, *8*, 1837–1866. [CrossRef]
9. Wang, H.; Zhu, Q.-L.; Zou, R.; Xu, Q. Metal-Organic Framewors for Energy Applications. *Chem* **2017**, *2*, 52–80. [CrossRef]
10. Tylianakis, E.; Klontzas, E.; Froudakis, G.E. The effect of structural and energetic parameters of MOFs and COFs towards the improvement of their hydrogen storage properties. *Nanotechnology* **2009**, *20*, 204030. [CrossRef] [PubMed]
11. Toyao, T.; Saito, M.; Horiuchi, Y.; Mochizuki, K.; Iwata, M.; Higashimura, H.; Matsuoka, M. Efficient hydrogen production and photocatalytic reduction of nitrobenzene over a visible-light-responsive metal-organic framework photocatalyst. *Catal. Sci. Technol.* **2013**, *3*, 2092–2097. [CrossRef]
12. Li, D.; Xu, H.-Q.; Jiao, L.; Jiang, H.-L. Metal-organic frameworks for catalysis: State of the art, challenges, and opportunities. *EnergyChem* **2019**, *1*, 100005. [CrossRef]

13. Llabres, F.X.; Luz, I.; Ciruyano, F.G. Strategies of Creating active Sites in MOF. In *Metal Organic Frameworks as Heterogeneous Catalysts*, 1st ed.; Llabres, F.X., Gascon, J., Eds.; The Royal Society of Chemistry: Cambridge, UK, 2007; pp. 238–267.
14. Blake, A.J.; Champness, N.R.; Easun, T.L.; Allan, D.R.; Nowell, H.; George, M.W.; Jia, J.; Sun, X.-Z. Photoreactivity examined through incorporation in metal organic frameworks. *Nat. Chem.* **2010**, *2*, 688–694. [CrossRef]
15. Wang, C.; Xie, Z.; deKrafft, K.E.; Lin, W.J. Doping Metal-Organic Frameworks for Water Oxidation, Carbon Dioxide reduction, and Organic Photocatalysis. *J. Am. Chem. Soc.* **2011**, *133*, 13445–13454. [CrossRef] [PubMed]
16. Choi, K.M.; Kim, D.; Rungtaweevoranit, B.; Trickett, C.A.; Barmanbek, J.T.D.; Alshammari, P.Y.; Yaghi, O.M. Plasmon-Enhanced Photocatalytic CO_2 Conversion within Metal-Organic Frameworks under Visible Light. *J. Am. Chem. Soc.* **2017**, *139*, 356–362. [CrossRef] [PubMed]
17. Kaskel, S. *The Chemistry of Metal-Organic Frameworks: Synthesis, Characterization and Application*, 7th ed.; John Wiley & Sons Incorporated: Weinheim, Germany, 2016; pp. 5–37.
18. Cavka, J.H.; Jakobsen, S.; Olsbye, U.; Guillou, N.; Lamberti, C.; Bordiga, S.; Lillerud, K.P. A new zirconium inorganic building brick forming metal organic frameworks with exceptional stability. *J. Am. Chem. Soc.* **2008**, *130*, 13850–13851. [CrossRef] [PubMed]
19. Cliffe, M.J.; Wan, W.; Zou, X.; Chater, P.A.; Kleppe, A.A.; Tucker, M.G.; Wilhelm, H.; Funnell, N.P.; Coudert, F.-X.; Goodwin, A.L. Correlated defect nanoregions in a metal-organic framework. *Nat. Commun.* **2014**, *5*, 4176. [CrossRef]
20. Hu, Z.; Zhao, D. De facto methodologies toward the synthesis and scale-up production of UiO-66-type metal-organic frameworks and membrane materials. *Dalton Trans.* **2015**, *44*, 19018–19040. [CrossRef] [PubMed]
21. Jakobsen, S.; Gianolio, D.; Wragg, D.S.; Nilsen, M.H.; Emerich, H.; Bordiga, S.; Lamberti, C.; Olsbye, U.; Tilset, M.; Lillerud, K.P. Structural determination of a highly stable metal-organic framework with possible application to interim radioactive waste scavenging Hf-UiO-66. *Phys. Rev. B Condens. Matter Mater. Phys.* **2012**, *86*, 125429. [CrossRef]
22. Wu, X.P.; Gagliardi, L.; Truhlar, D.G. Cerium Metal-Organic framework for Photocatalysis. *J. Am. Chem. Soc.* **2018**, *140*, 7904–7912. [CrossRef]
23. Hosono, N.; Kitagawa, S. Modular Desigh of Porous Soft Materials via Self-Organization of Metal-Organic Cages. *Acc. Chem. Res.* **2018**, *51*, 2437–2446. [CrossRef] [PubMed]
24. Yeung, H.H.-M.; Yoshikawa, G.; Minami, K.; Shiba, K. Strain-based chemical sensing using metal-organic framework nanoparticles. *J. Mater. Chem. A* **2020**, *8*, 18007–18014. [CrossRef]
25. Musho, T.; Li, J.; Wu, N. Band Gap modulation of functionalized metal-organic frameworks. *Phys. Chem. Chem. Phys.* **2014**, *16*, 23646–23653. [CrossRef] [PubMed]
26. Ganose, A.M.; Jackson, A.J.; Scanlon, D.O. sumo: Command-line tools for plotting and analysis of periodic ab initio calculations. *J. Open Source Softw.* **2018**, *3*, 717. [CrossRef]
27. Pu, S.; Xu, L.; Sun, L.; Du, H. Tuning the optical properties of the zirconium–UiO-66 metal–organic framework for photocatalytic degradation of methyl orange. *Inorg. Chem. Commun.* **2015**, *52*, 50–52. [CrossRef]
28. Parsons, R.; Bard, A.J.; Parsons, R.; Jordan, J. *Standard Potentials in Aqueous Solution*, 1st ed.; M. Dekker: New York, NY, USA, 1985; pp. 13–37.
29. Donald, W.A.; Leib, R.D.; O'Brien, J.T.; Bush, M.F.; Williams, E.R. Absolute Standard Hydrogen Electrode Potential Measured by Reduction of Aqueous Nanodrops in the Gas Phase. *J Am Chem Soc.* **2008**, *130*, 3371–3381. [CrossRef]
30. Kresse, G.; Hafner, J. Ab initio molecular dynamics for liquid metal. *Phys. Rev. B.* **1993**, *47*, 558–561. [CrossRef]
31. Kresse, G.; Hafner, J. Ab initio molecular-dynamics simulation of the liquid-metalamorphous- semiconductor transition in germanium. *Phys. Rev. B.* **1994**, *49*, 14251–14269. [CrossRef]
32. Kresse, G.; Furthmüller, J. Efficiency of ab-initio total energy calculations for metals and semiconductors using a plane-wave basis set. *Comput. Mater. Sci.* **1996**, *6*, 15–50. [CrossRef]
33. Kresse, G.; Furthmüller, J. Efficient iterative schemes for ab initio total-energy calculations using a plane-wave basis set. *Phys. Rev. B* **1996**, *54*, 11169–11186. [CrossRef]
34. Perdew, J.P.; Burke, K.; Ernzerhof, M. Generalized Gradient Approximation Made Simple. *Phys. Rev. Lett.* **1996**, *77*, 3865–3868. [CrossRef] [PubMed]
35. Blöchl, P.E. Projector augmented-wave method. *Phys. Rev. B.* **1994**, *50*, 17953–17979. [CrossRef]
36. Kresse, G.; Joubert, D. From ultrasoft pseudopotentials to the projector augmented-wave method. *Phys. Rev. B Condens. Matter Mater. Phys.* **1999**, *59*, 1758–1775. [CrossRef]
37. Dudarev, S.L.; Botton, G.A.; Savrasov, S.Y.; Humphreys, C.J.; Sutton, A.P. Electron-energy-loss spectra and the structural stability of nickel oxide: An LSDA+U study. *Phys. Rev. B* **1998**, *57*, 1505. [CrossRef]
38. Blöchl, P.E.; Jepsen, O.; Andersen, O.K. Improved tetrahedron method for Brillouin-zone integrations. *Phys. Rev. B* **1994**, *49*, 16223. [CrossRef] [PubMed]
39. Butler, K.T.; Hendon, C.H.; Walsh, A. Electronic chemical potentials of porous metal-organic frameworks. *J. Am. Chem. Soc.* **2014**, *136*, 2703–2706. [CrossRef]
40. Gajdoš, M.; Hummer, K.; Kresse, G.; Furthmüller, J.; Bechstedt, F. Linear optical properties in the projector-augmented wave methodology. *Phys. Rev. B* **2006**, *73*, 045112. [CrossRef]
41. Momma, K.; Izumi, F. VESTA: A three-dimensional visualization system for electronic and structural analysis. *J. Appl. Crystallogr.* **2008**, *41*, 653–658. [CrossRef]